




# Catching profound optical flares in blazars

Gopal Bhatta <sup>1</sup>★, Staszek Zola <sup>2</sup>, M. Drozd,<sup>3</sup> Daniel Reichart,<sup>4</sup> Joshua Haislip,<sup>4</sup> Vladimir Kouprianov,<sup>4</sup> Katsura Matsumoto,<sup>5</sup> Eda Sonbas,<sup>6,7</sup> D. Caton,<sup>8</sup> Urszula Pajdosz-Śmierciak,<sup>2</sup> A. Simon,<sup>9</sup> J. Provencal,<sup>10,11</sup> Dariusz Góra <sup>1</sup> and Grzegorz Stachowski<sup>2</sup>

<sup>1</sup>*Institute of Nuclear Physics Polish Academy of Sciences, PL-31342 Kraków, Poland*

<sup>2</sup>*Astronomical Observatory of the Jagiellonian University, ul. Orla 171, PL-30-244 Kraków, Poland*

<sup>3</sup>*Mt. Suhora Observatory, Pedagogical University, ul. Podchorążych 2, PL-30-084 Kraków, Poland*

<sup>4</sup>*Dept. of Physics and Astronomy, University of North Carolina at Chapel Hill, Chapel Hill, NC 27599, USA*

<sup>5</sup>*Astronomical Institute, Osaka Kyoiku University, 4-698 Asahigaoka, Kashiwara, Osaka 582-8582, Japan*

<sup>6</sup>*University of Adiyaman, Department of Physics, 02040 Adiyaman, Turkey*

<sup>7</sup>*Astrophysics Application and Research Center, Adiyaman University, Adiyaman 02040, Turkey*

<sup>8</sup>*Dark Sky Observatory, Department of Physics and Astronomy, Appalachian State University, Boone, NC 28608, USA*

<sup>9</sup>*Astronomy and Space Physics Department, Taras Shevchenko National University of Kyiv, Volodymyrska str. 60, UA-01033 Kyiv, Ukraine*

<sup>10</sup>*University of Delaware, Department of Physics and Astronomy Newark, DE 19716, USA*

<sup>11</sup>*Delaware Asteroseismic Research Center, Mt. Cuba Observatory, Greenville, DE 19807, USA*

Accepted 2023 January 23. Received 2023 January 12; in original form 2022 September 8

## ABSTRACT

Flaring episodes in blazars represent one of the most violent processes observed in extra-galactic objects. Studies of such events shed light on the energetics of the physical processes occurring in the innermost regions of blazars, which cannot otherwise be resolved by any current instruments. In this work, we present some of the largest and most rapid flares captured in the optical band in the blazars 3C 279, OJ 49, S4 0954+658, TXS 1156+295, and PG 1553+113. The source flux was observed to increase by nearly ten times within a time-scale of a few weeks. We applied several methods of time series analysis and symmetry analysis. Moreover, we also performed searches for periodicity in the light curves of 3C 279, OJ 49 and PG 1553+113 using the Lomb–Scargle method and found plausible indications of quasi-periodic oscillations (QPOs). In particular, the 33- and 22-day periods found in 3C 279, i.e. a 3:2 ratio, are intriguing. These violent events might originate from magnetohydrodynamical instabilities near the base of the jets, triggered by processes modulated by the magnetic field of the accretion disc. We present a qualitative treatment as the possible explanation for the observed large amplitude flux changes in both the source-intrinsic and source-extrinsic scenarios.

**Key words:** radiation mechanisms: non-thermal – relativistic processes – galaxies: active – BL Lacertae objects: individual.

## 1 INTRODUCTION

Blazars are a sub-class of radio-loud active galactic nuclei (AGN) featuring relativistic jets which are closely aligned to the line of sight (Urry & Padovani 1995). The blazar continuum emission is non-thermal in nature, and it is DOPPLER boosted and highly variable over a wide range of spatial and temporal frequencies. Blazars consist of two kinds of sources: flat-spectrum radio quasars (FSRQ) and BL Lacertae (BL Lac) objects. Of the two types of sources, FSRQs show broad emission lines, while BL Lacs exhibit either weak emission lines or their absence over the continuum. None the less, the objects are visible in the TeV energy range and constitute the dominant population of discrete gamma-ray sources in the sky. Historically, FSRQs are considered to be more luminous than BL Lacs, however, new reports suggest that some of the BL Lacs can be more luminous than FSRQs (see Sheng et al. 2022). The broad-band non-thermal

spectrum of blazars, which extends from radio to the highest energy  $\gamma$ -rays such as TeV emission, exhibits two distinct low- and high-energy components which respectively peak between radio and soft X-rays and between X-rays and  $\gamma$ -rays. The low-energy component is well explained in terms of synchrotron emission by relativistic plasma in the magnetized jets. However, various models, mainly leptonic or hadronic scenarios, have been put forward to explain the origin of high-energy emission. According to the leptonic scenario, ultra-relativistic electrons up-scatter low-energy seed photons into X-rays and  $\gamma$ -rays via the inverse-Compton mechanism. Further, in the synchrotron self-Compton (SSC; e.g. Marscher & Gear 1985; Maraschi, Ghisellini & Celotti 1992) model, the synchrotron photons produced by the electrons constitute a radiation field which is inverse-Compton scattered by the co-spatial leptons. In the external Compton (EC) models, AGN components such as the accretion disc, broad-line region, and dusty torus (Dermer, Schlickeiser & Mastichiadis 1992; Sikora, Begelman & Rees 1994; Ghisellini & Madau 1996) could contribute the low-energy seed photons required for the inverse-Compton scattering. Conversely, the hadronic models suggest that the

\* E-mail: [gopal.bhatta@ifj.edu.pl](mailto:gopal.bhatta@ifj.edu.pl)

protons may be accelerated to very high energies, which then produce the high-energy spectral component via direct proton-synchrotron and/or photon-initiated cascades (Mannheim 1993; Aharonian 2000; Mücke et al. 2003). Although both leptonic and hadronic models can account for the origin of high-energy emission from blazars, the hadronic models require a stronger magnetic field to radiatively cool more massive protons. Similarly, the proton-synchrotron models also require the acceleration of ultra high energy cosmic rays (UHECRs) in the blazar jets, which trigger photo-pionic interactions resulting in gamma-ray emission along with some secondary particles. In such interactions, neutrino production in the jets becomes a natural outcome. Indeed, the IceCube (IceCube Collaboration 2018) experiment detected high energy neutrinos potentially associated with gamma-ray flaring in the blazar TXS 0506 + 056.

Blazars are characterized by multiwavelength (MWL) flux variability over diverse time-scales (e.g. see Bhatta et al. 2016a; Bhatta, Mohorian & Bilinsky 2018; Bhatta & Webb 2018; Bhatta & Dhital 2020; Bhatta 2021). Although the statistical variability properties can be largely represented by a single power-law spectral density (see optical; Nilsson et al. 2018; and  $\gamma$ -ray; Bhatta & Dhital 2020), blazars often display complex variability patterns, such as red-noise like variability superimposed by occasional sharp rises in the flux. In the majority of the cases, such rises in flux possess a well-defined shape and last for a definite duration and therefore, can be identified as distinct flaring events, which can either be observed simultaneously in MWL observations (e.g. Aleksić et al. 2015; Hayashida et al. 2015; Baloković et al. 2016; Abeysekara et al. 2018; Acciari et al. 2020) or only in a specific wavelength band, often termed as ‘orphan’ flares, (e.g. see Chatterjee et al. 2013, for optical orphan flares). Some of the dominant flaring events, which show a large rise in the flux, typically last from a few weeks to months. These events suggest the presence of extreme physical conditions prevalent around the central engine as well as in the jets, which may drive the most efficient particle acceleration and cooling processes. In the gamma-ray domain, blazar flaring episodes are often accompanied by a large swing in the rotation of the plane of optical polarization (Blinov et al. 2018), consistent with the violent collision between the relativistic shock waves and stationary structures such as Mach disc. Moreover, such events are also seen to be accompanied by the ejection of radio knots seen in Very Long Baseline Array images (Marscher et al. 2010; Park et al. 2019). Studies of blazar radio jets seem to indicate that, in most cases, flaring events in blazars can be linked with disturbances propagating along the jet, which lead to the ejection of radio knots showing apparent superluminal motion (Jorstad et al. 2001; Kellermann et al. 2004; Jorstad & Marscher 2016). In the case of weakly magnetized jets, the shock waves propagating along the jet can energize the particles to induce the flaring events (Lind & Blandford 1985). On the other hand, if the jets are highly magnetized, magnetic reconnection might play a dominant role in particle acceleration (Nalewajko et al. 2011; Giannios 2013) before energy dissipation. Also, the re-collimation of the shock waves can lead to the formation of rapid flares (Bromberg & Levinson 2009).

In this work, we present the results of our analysis of flaring observations of five blazars obtained by our group in the course of long-term optical monitoring of AGN. In Section 2, the observations of the source sample and the relevant optical data processing are described. A brief description of each of the sample sources is presented in Section 3. In Section 4, several analytical approaches using various methods, including fractional variability (FV), flux distribution, PSD and QPOs, are introduced, and the results of the analyses of the light curves are presented. The results, along with their

possible implications, are discussed in Section 5, and we summarize our conclusions in Section 6.

## 2 OBSERVATIONS AND DATA PROCESSING

Long term monitoring of a sample of quasars was primarily carried out using small telescopes operated by the Skynet Robotic Telescope Network (Zola et al. 2021). Additional data were collected with the 60 cm telescope located at Adiyaman University Astrophysics Application and Research Center, Turkey, the 50 cm telescope at the Osaka University Observatory in Japan, and with two telescopes in Poland: A 60 cm at the Mt. Suhora Observatory and a 50 cm at the Jagiellonian University Observatory in Krakow. The wide band R filter (Bessell prescription) was most often used for the monitoring. Longer runs were also carried out, mostly at the Krakow and Mt. Suhora sites.

The data taken by Skynet consists of several scientific images of a target taken each night, subsequently reduced for bias, dark and flat-field by the network pipeline. Other sites provided raw images accompanied by calibration frames. We performed reduction of raw images with the standard procedure: Calibration for bias, dark and flat-field (usually taken on the sky) with the IRAF package, while extraction of magnitudes was done using aperture photometry with the CMunipack program, which implements the DAOPHOT algorithm. As a result, differential magnitudes were derived with comparison stars for each object chosen so as to be visible in the field of view of all telescopes. Their constancy was verified with check stars which were similarly chosen. The sample of sources along with their classes, positions, and red-shifts are presented in Table 1, which also lists the blazar source classification based on synchrotron peak frequency, that is, high synchrotron peaked blazars (HSP;  $\nu_{\text{peak}}^S > 10^{15}$  Hz), intermediate synchrotron peaked blazars (ISP;  $10^{14} < \nu_{\text{peak}}^S < 10^{15}$  Hz), and low synchrotron peaked blazars (LSP;  $\nu_{\text{peak}}^S < 10^{14}$  Hz) (Abdo et al. 2010a). Similarly, for a given source, the total observation duration, the number of observations and the mean magnitude are listed in the 2nd, 3rd, and 4th columns, respectively, of Table 2.

## 3 SOURCE DESCRIPTION

### 3.1 OJ 49

Blazar OJ 49 is a BL Lac object located at a redshift of 0.17386. The Very Large Array (VLA) radio image of the source at 20 cm (Antonucci & Ulvestad 1985) shows a sharply curved extending jet, while a 43 GHz Very Long Baseline Array (VLBA) image shows a highly polarized jet extending about 0.6 mas from the core (Lister, Marscher & Gear 1998). Similarly, VLBA images at 22 GHz revealed prominent jet ejecting knotty components at apparently superluminal speeds (Jorstad et al. 2001). During VLBI Space Observatory Program mission, the core size of the 5 GHz radio emission was estimated to be 0.5 mas (Dodson et al. 2008). In the optical and near-IR bands, the blazar exhibits strong intraday variability of polarization and total flux (see Sitko, Schmidt & Stein 1985; Smith et al. 1987).

### 3.2 S4 0954+658

BL Lac S4 0954+658 is known to display significant flux and polarization variability on both intra-day and longer time-scales. Long-term optical variability of the source by Raiteri et al. (1999) showed large amplitude-flux modulations. Similarly, Papadakis et al. (2004) made multiband optical observations of the source for a few nights and found the source to be variable by  $< 5$  percent within

**Table 1.** General information about the sample of blazar targets.

Source name	Source class	R.A. (J2000)	Dec. (J2000)	Redshift ( $z$ )
OJ 49	BL Lac, LSP	08 <sup>h</sup> 31 <sup>m</sup> 48.88 <sup>s</sup>	+04 <sup>d</sup> 29 <sup>m</sup> 39.086 <sup>s</sup>	0.17386
S4 0954+658	BL Lac, LSP	09 <sup>h</sup> 58 <sup>m</sup> 47.2 <sup>s</sup>	+65 <sup>d</sup> 33 <sup>m</sup> 55 <sup>s</sup>	0.368
TXS 1156+295	FSRQ, LSP	11 <sup>h</sup> 59 <sup>m</sup> 032.07 <sup>s</sup>	+29 <sup>d</sup> 14 <sup>m</sup> 42.0 <sup>s</sup>	0.729
3C 279	FSRQ, LSP	12 <sup>h</sup> 56 <sup>m</sup> 11.1665 <sup>s</sup>	−05 <sup>d</sup> 47 <sup>m</sup> 21.523 <sup>s</sup>	0.536
PG 1553+113	BL Lac, HSP	15 <sup>h</sup> 55 <sup>m</sup> 43.044 <sup>s</sup>	+11 <sup>d</sup> 11 <sup>m</sup> 24.365 <sup>s</sup>	0.36

**Table 2.** Optical observations of a sample of blazars and their variability properties.

Source name (1)	Duration (d) (2)	Npt. (3)	mean mag (4)	VA (mag) (5)	Fvar (%) (6)	$t_{\text{var}}$ (min.) (7)	$t_r$ (d) (8)	$t_d$ (d) (9)
OJ 49	164.28	620	16.28	2.75	66.23 ± 0.24	38.24 ± 11.80	0.57	0.44
TXS 1156+295	79.65	650	17.45	3.30	62.78 ± 0.13	19.06 ± 13.73	-	4.10
PG 1553+113	97.43	1071	15.57	0.91	23.61 ± 0.21	64.76 ± 11.18	-	-
3C 279	461.58	1831	17.59	2.78	46.16 ± 0.50	11.73 ± 7.80	-	-
S4 0954+658	242.70	2988	14.80	2.61	47.60 ± 0.17	17.10 ± 6.18	3.05	5.15

the observational period. Morozova et al. (2014) studied the MWL behaviour of S4 0954+658 during a powerful outburst in 2011 March–April using optical (R-band) photometric and polarimetric monitoring and VLBA observations. The authors reported an increase of the flux by 2.8 mag within a period of two months and a steep intra-night flux increase of  $\sim 0.7$  mag. Similarly, in a study involving multicolour photometric and polarization observations of the blazar during 2008–2012, the source revealed a power-law spectrum and high degree of polarization, confirming the synchrotron nature of the emission (Hagen-Thorn et al. 2015). The source also displayed significant colour variability with a trend of bluer-when-brighter (BWB). Morozova et al. (2016) investigated the behaviour of the source during the outburst in early 2015 using observations from cm-wave to  $\gamma$ -ray energies. It was found that the optical flaring coincided with a similar flare observed in  $\gamma$ -rays. During the same period, very-high-energy  $\gamma$ -ray emission was detected and the ejection of a new, bright polarized superluminal knot was observed by the VLBA at 43 GHz. More recently, Vlasyuk et al. (2022) reported the fastest fall in the source’s optical flux, by  $\sim 0.25$  mag, within 15 minutes, accompanied by a minute-time-scale QPO.

### 3.3 TXS 1156+295

Blazar TXS 1156+295, also known as Ton 599 and as 4FGL J1159.5+2914 in the *Fermi*-LAT 4th catalogue, is an FSRQ situated at the position of R.A. = 11<sup>h</sup>59<sup>m</sup>31.8<sup>s</sup> and Dec. = + 29°14′43″8 and lies at a redshift  $z = 0.725$  (Hewett & Wild 2010). The source was first detected in the  $\gamma$ -ray band by the Energetic Gamma Ray Experiment Telescope (EGRET) and later was also detected in very high-energy emission ( $> 100$  GeV) by VERITAS (Mukherjee & VERITAS Collaboration 2017). In the optical band, the blazar is highly variable in all time-scales. Fan et al. (2006) presented a study of the sources using photometric observations, which showed a large variation ( $\Delta m \sim 5.8$  mag) in the optical flux on time-scales of a few years. In 2017, the source was reported to have undergone optical flaring (Pursimo et al. 2017). In the  $\gamma$ -ray band, power spectral density (PSD) and flux distribution analysis of decade-long *Fermi*/LAT observations were carried out by Bhatta & Dhital (2020). More recently, Rajput & Pandey (2021) studied the flux and spectral variability of the source during its  $\gamma$ -ray flaring in 2021. Also, the variability of the emission-line during a non-thermal outburst was reported by Hallum et al. (2022).

### 3.4 3C 279

Blazar 3C 279 is an FSRQ source profusely emitting in hard X-rays and  $\gamma$ -rays. Highly variable across a wide range of spectral bands (see Hayashida et al. 2015; Paliya et al. 2016, and the references therein), it is one of the few FSRQs detected above 100 GeV (MAGIC Collaboration 2008). The source reveals a compact, milliarcsecond-scale radio core ejecting radio knots with a bulk Lorentz factor  $\Gamma = 15.5 \pm 2.5$ , in a direction making an angle  $\theta_{\text{obs}} = 2.1 \pm 1.1^\circ$  to the line of sight (Jorstad et al. 2004, 2005). During Whole Earth Blazar Telescope (WEBT) campaigns, the source flux in the optical was reported to undergo an exponential-type decay on a time-scale of  $\sim 10$  d (Böttcher et al. 2007). Similarly, Larionov et al. (2008) in another WEBT campaign in 2006–2007 observed a slower but large flux decline,  $\sim 3$  mag on a time-scale of  $\sim 100$  d, in the optical and near-IR band. Bhatta et al. (2018) discussed the flux and spectral variability properties of the source in the hard X-ray band during intra-day time-scales. More recently, Agarwal et al. (2019) presented multiband optical variability of the source and found that large amplitude variability within a time-scale of a few months and a mild BWB trend on shorter time-scales. The optical observations of this source are presented in the bottom panels of Fig. 1. A sharp fall in the flux ( $\Delta m \sim 2.0$ ) within a time-scale of 100 d is separately shown in the right-hand panel.

### 3.5 PG 1553+113

Blazar PG 1553+113 is a BL Lac source which has been studied from radio to  $\gamma$ -rays in different observation campaigns (e.g. Osterman et al. 2006; Ackermann et al. 2015; Raiteri et al. 2015, 2017). The source is famous for its  $\sim 2.18$  yr periodicity, first revealed in *Fermi*/LAT observations (Ackermann et al. 2015). It was classified as a BL Lac object based on its featureless spectrum (Falomo & Treves 1990) and was further sub-classified as a high-peaked BL Lac (HBL) object (see Beckmann et al. 2002, and references therein). Evidence of very-high-energy  $\gamma$ -ray emission from this source was first reported by H.E.S.S. in 2005 (Aharonian et al. 2006) and was later confirmed by observations above 200 GeV with the MAGIC telescope at a significance level of  $8.8\sigma$  (Albert et al. 2007). Due to its featureless optical spectrum, the redshift of PG 1553+113 remains highly uncertain. Measurements using the Cosmic Origins Spectrograph onboard the *Hubble Space Tele-*

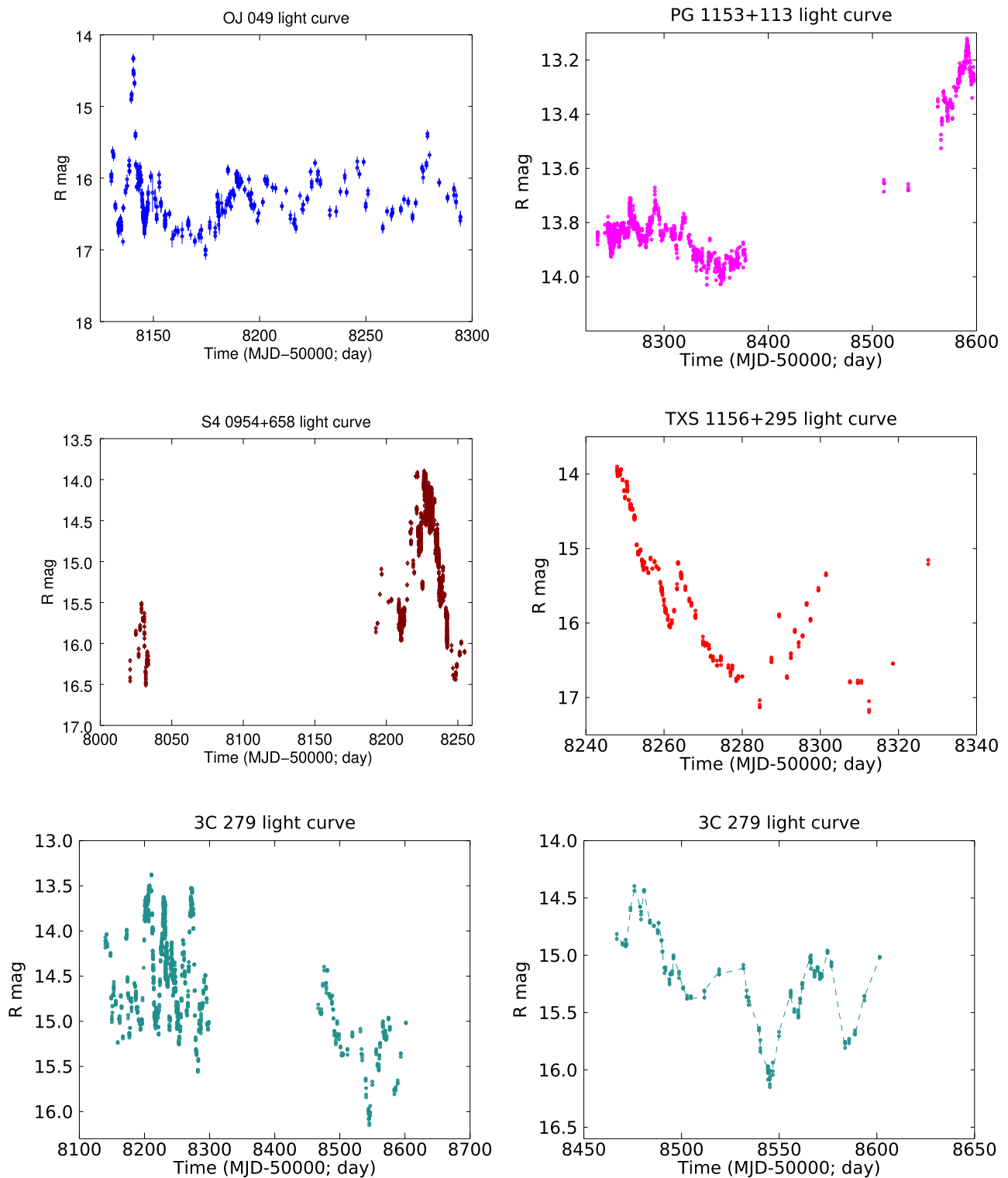


**Figure 1.** Optical (R-band) observations of the sample of blazars.

*scope* yielded a lower limit of 0.395 (Danforth et al. 2010). The small statistical uncertainties of the VERITAS energy spectrum help constrain the upper limit of the redshift to a value of  $\sim 0.62$  (Aliu et al. 2015). During multifrequency WEBT campaign in 2013 April–August, the source was found to display a general BWB trend in the optical regime (Raiteri et al. 2015). Meng et al.

(2018) studied the source using the optical multiband observations in the yearly time-scale. During the observation period the source exhibited moderately varying multiband emission, without any inter-band lag. Pandey et al. (2019) reported variable emission in the optical V and R bands with a mean optical spectral index of  $\sim 0.83 \pm 0.21$ .



## 4 ANALYSIS AND RESULTS

In order to characterize the properties of the flaring episodes in the target sources, we analysed the optical observations through multiple analysis methods. The methods and results of the analyses for the individual sources are presented below.

### 4.1 Variability measures and time-scales

In order to obtain a quantified measure of the observed variability in the sources, the following three measures of variability are estimated. Variability amplitude (VA) as given in Heidt & Wagner (1996) provides an measure of the net flux change during the observation period and is written as

$$VA = \sqrt{(A_{\max} - A_{\min})^2 - 2\sigma^2}, \quad (1)$$

where  $A_{\max}$  and  $A_{\min}$  are the maximum and minimum of the source magnitude, respectively, and  $\sigma$  represents mean error in the magnitude measurements. The VA of the sample sources are listed in Table 2. Subsequently, the VA in magnitudes then can be directly converted into flux ratio using the relation  $f_1/f_2 = 10^{-0.4(m_1 - m_2)}$ , where  $m_1$  and  $m_2$  are the initial and final magnitudes of the variable source. This allows us to compute the factor by which the flux changed during the observational period.

We observed high-amplitude rapid variability in the blazars included in our study. As seen in Fig. 1, and also indicated by the VA (in magnitudes) listed in the 5th column of Table 2, the optical flux of blazar 3C 279 was observed to change by  $\sim 13$  times within a time-scale of a few hundred days. Similarly, in OJ 49, we measured a flux change by a factor of  $\sim 12$  within the period of  $\sim 12$  d, as shown in the top panel of Fig. 1 and in TXS 1156+295 by a factor of  $\sim 16$  within a time-scale of  $\sim 22$  d, as seen in the middle panel of Fig. 1. Likewise, the optical light curve showing flux modulation in the blazar PG 1553+113 is presented in the top right panel of Fig. 1.

The VA considers only extreme values and therefore provides a measure for the peak-to-peak magnitude change. Average variability during the entire period can be quantified by estimating their FV given as

$$F_{var} = \sqrt{\frac{S^2 - \langle \sigma_{err}^2 \rangle}{\langle F \rangle^2}}, \quad (2)$$

where  $S^2$  and  $\langle \sigma_{err}^2 \rangle$  represent the variance and the mean of the squared measurement errors, respectively; and the uncertainty in FV can be expressed as

$$\sigma_{F_{var}} = \sqrt{F_{var}^2 + \sqrt{\frac{2}{N} \frac{\langle \sigma_{err}^2 \rangle^2}{\langle F \rangle^4} + \frac{4}{N} \frac{\langle \sigma_{err}^2 \rangle}{\langle F \rangle^2} F_{var}^2} - F_{var}} \quad (3)$$

(Vaughan et al. 2003, see also Bhatta & Webb 2018). The FV values for the sample sources are listed in the 6th column of Table 2, which show large average flux variability during the period.

The variability time-scale ( $\tau_{var}$ ) can be taken as the e-folding time-scale of flux change given by

$$\tau_{var} = \left| \frac{\Delta t}{\Delta \ln F} \right|, \quad (4)$$

(Burbidge, Jones & Odell 1974, see also Bhatta et al. 2018), where  $\Delta t$  is the time interval corresponding to the change in natural logarithm of flux measurements. Using the above relation,  $\tau_{var}$  of the sample light curves are calculated and listed in the 7th column of Table 2. Of the sample sources, a shortest  $\tau_{var}$  of 11 min is observed blazar 3C

279, whereas the source PG 1553+113 appears to show relatively slower variability with a  $\tau_{var}$  of 65 min.

Rapid variability in shorter time-scales can be associated with the synchrotron cooling time-scales, which can be expressed as,

$$t_{cool} \sim 7.74 \times 10^8 \gamma^{-1} B^{-2} \text{ s}, \quad (5)$$

where  $\gamma$  and  $B$  represent electron Lorentz factor and ambient magnetic field, respectively. Also, we use  $\beta \sim 1$  considering ultra-relativistic electrons (see also Bhatta et al. 2018). Using a typical jet magnetic field of 1 Gauss and a minimum variability time-scale of 30 min, the energy of the relativistic electrons emitting optical synchrotron emission can be estimated to  $\sim 3 \times 10^5$  Lorentz factors. Moreover, following the causality argument, the time-scale  $\tau_{var}$  can be used to estimate the upper limit for the minimum size of the emitting region ( $R$ ) as given by  $R \geq \frac{\delta}{(1+z)} c \tau_{var}$ ; where  $\delta$ , Doppler factor, is defined as  $\delta = (\Gamma(1 - \beta \cos \theta))^{-1}$ , and for the velocity  $\beta = v/c$  the bulk Lorentz factor can be written as  $\Gamma = 1/\sqrt{1 - \beta^2}$ . If we use a typical value of Doppler factor of 10 and  $z = 0.5$ , a 30 min minimum variability time-scale could have arisen from a region that is 1/1000th of a parsec in scale.

### 4.2 Symmetry analysis: rise and decay profiles

The rise and decay profiles of flares in blazar light curves can be associated with the particle acceleration and cooling time-scales, respectively, and thereby can be linked to the physical processes leading to the flaring episodes. To characterize the flaring properties, we performed symmetry analysis of the flares. For that purpose, we took parts of the light curves of the sources OJ 49, S4 0954+658, and TXS 1156+295 (see Fig. 1) which showed well resolved flares, with a well-defined generally monotonic rise and decay, and the three flares were fitted by a functional form representing the temporal structure of the exponential rise and decay described by

$$F(t) = F_c + F_0 \left[ e^{\frac{t_0 - t}{t_r}} + e^{\frac{t - t_0}{t_d}} \right]^{-1}, \quad (6)$$

where  $F_c$  is the constant flux level,  $F_0$  is the amplitude of the flaring structure and  $t_0$  the centre of the flare, and  $t_r$  and  $t_d$  are the rise and decay times of the flares (Abdo et al. 2010b). The parts of the light curves of the sources which show distinct flares and the corresponding functional fits are shown in Fig. 2. The rise and decay time-scales determined from the fitting are listed in the 8th and 9th columns, respectively, of Table 2. Using the obtained time-scales, a symmetry parameter written as  $\xi = (t_d - t_r)/(t_d + t_r)$  can be defined within  $[-1, 1]$  such that  $\xi = -1, +1$  represent completely right- and left-asymmetric flares, whereas  $\xi = 0$  represents completely symmetric flares. The asymmetry parameters for OJ 49 and S4 0954+658  $\xi = 0.13$  and  $\xi = -0.25$ , respectively. The result indicates that the flares in these sources are, respectively, slightly left- and right-asymmetric. Since the source TXS 1156+295 was only observed during its decay phase, its  $\xi$  could not be estimated. Also, although the amplitude of the flares in OJ 49 and S4 0954+658 are similar, with normalized amplitudes ( $F_0/F_c$ ) = 8.5 and 8.2 respectively, the rise and decay times are considerably shorter in OJ 49, indicating fast flaring events. In the case of TXS 1156+295, an even faster decay of flux, by 11.3 normalized amplitudes, is observed within 4.3 d.

### 4.3 Periodicity analysis

QPOs in blazars with characteristic time-scales of a few years have been frequently reported (Bhatta et al. 2016b, see also Zola et al.

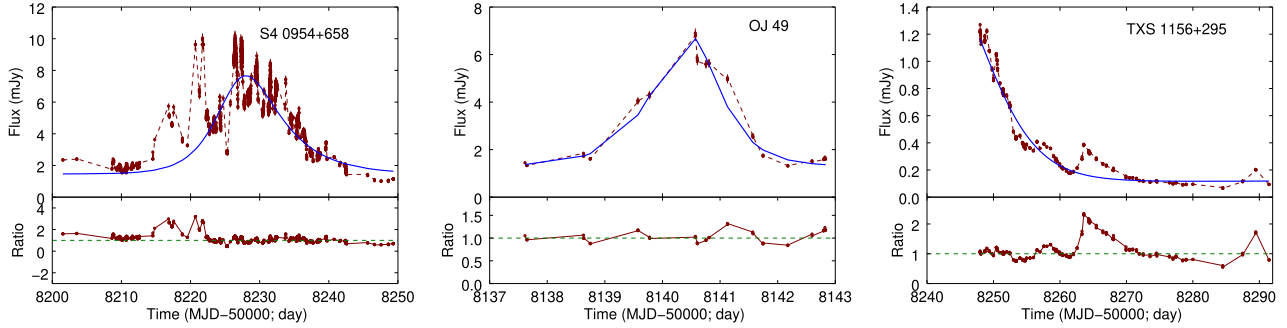


**Figure 2.** Fitting of the flares observed in optical (R-band) observations of the sample blazars with a curve (shown in blue colour) parametrized with an exponential rise and decay are presented in the upper panels of the figures. The lower panels show the ratio between the observations and the models. The corresponding rise and decay times from the best-fitting models are presented in the 8th and 9th columns of Table 2.

2016). However, not many blazar QPOs are observed on time-scales of a few days or weeks. We searched for the possible periodic flux modulations in the optical bands using Lomb–Scargle method (Lomb 1976; Scargle 1982). The method modifies the conventional discrete Fourier periodogram such that the least-square fitting of sine waves of the form  $X_i(t) = A \cos \omega t + B \sin \omega t$  to the data is minimized. The periodogram is given as

$$P = \frac{1}{2} \left\{ \frac{[\sum_i x_i \cos \omega(t_i - \tau)]^2}{\sum_i \cos^2 \omega(t_i - \tau)} + \frac{[\sum_i x_i \sin \omega(t_i - \tau)]^2}{\sum_i \sin^2 \omega(t_i - \tau)} \right\}, \quad (7)$$

where  $\tau$  is given by  $\tan(2\omega\tau) = \sum_i \sin 2\omega t_i / \sum_i \cos 2\omega t_i$ .

The Lomb–Scargle periodogram (LSP) of the source light curves of PG 1553+113 and 3C 279 are presented in the right-hand panels of Fig. 3 and similarly LSP of the source OJ 049 is presented in Fig. 4. The light curve of blazar PG 1553+113 shows peaks at the time-scales of  $7 \pm 0.8$ ,  $25 \pm 3$ , and  $59 \pm 7$  d, which possibly may be the signs of QPO. Similarly the LSP of the blazar 3C 279 shows two prominent peaks around the time-scales of 22 and 33 d. Furthermore, in the LSP of the source OJ 049 a prominent peak around 12 d time-scale is observed.

To compute the significance of the observed periodogram features in the source LSP, a large number of light curves were generated by Monte Carlo simulations, and their statistical properties were utilized. In particular, the source periodograms based on Discrete Fourier Transform (DFT) were linearly fit in the logarithmic frequency space to obtain the best representative model PSD using the method described in Vaughan (2005). To avoid artefacts associated with DFT, some of the data were linearly interpolated to create an evenly spaced sampling. Using the best-fit PSD model, 10 000 light curves mimicking the observations in duration and sampling rate were simulated, and the distribution of these simulated LSP periodograms was used to determine 90 and 99 per cent significance contours (for detail, see Bhatta et al. 2016b; Bhatta & Dhital 2020), shown in magenta and red curves in the corresponding LSP figures. It can be seen that only the 12 d period in the source OJ 049 appears at over the 99 per cent significance level, although the 7 d period in PG 1552+113 and the 22 and 33 d periods in the source 3C 279 are clearly observed. We note that in another blazar, Mrk 501, a QPO of a similar time-scale of 23 d has been reported previously (see Rieger & Mannheim 2000).

## 5 DISCUSSION

Blazars are found to be violently variable over all time-scales from a few minutes to decades. Apart from stochastic variability often represented by power-law PSD, blazar light curves frequently show MWL flaring events characterized by well-resolved trends of monotonic rise or decline of flux, which can last from a few weeks to months. Studies by several blazar monitoring groups are particularly focused on flares in gamma-rays, which are frequently associated with the ejection of radio knots visible in VLBA images (Agudo et al. 2011; Wehrle et al. 2012; Jorstad et al. 2013). There is growing evidence that flaring events observed in the gamma-ray wavelength range could be associated with superluminally moving features crossing stationary features along the jet; it has been found that a large number of flares occur in coincidence with the passage of superluminal knots through the millimetre-wave core (see Jorstad et al. 2017, and the references therein).

Flares can be explained in terms of the sudden enhancement of the blazar flux followed by a strong energy dissipation event. The particles are accelerated to high energies via a number of particle acceleration mechanisms. In the shock diffusive acceleration model, shock waves compress and order the upstream magnetic field, causing the particles to accelerate through the Fermi acceleration mechanism and subsequently leading to the formation of outbursts of synchrotron emission (Blandford & Eichler 1987; Hughes, Aller & Aller 1998). Similarly, in the turbulent jet models, the main jet can be thought of as being divided into a large number of sub-volumes moving relativistically in random directions (see e.g. Narayan & Piran 2012; Marscher 2014). In this scenario, the passage of shock waves in the turbulent flow of relativistic plasma can heat the particles by compressing the plasma, and subsequently, depending upon the size and direction of the motion one single turbulent cell can beam dominantly to appear as a flare. In the case that the jet is highly magnetized, the turbulence can trigger intermittent magnetic instabilities, such as kink instabilities (Spruit, Daigne & Drenkhahn 2001) or inversions of the magnetic field near the base of the jet (Giannios & Uzdensky 2019), which lead to magnetic reconnection events and consequently acceleration of the particles to high energies (Guo, Sironi & Narayan 2014a, b). Similarly, magnetic reconnection events lead to the formation of plasmoids, which can grow to produce rapid flares with distinct and resolved envelopes. In this study, the flare is found to be slightly asymmetrical, which might suggest that the observed skewness in the flare profiles can be linked to both disturbance passing through the emission region and/or geometric effects such as those resulting from light crossing time. The origin

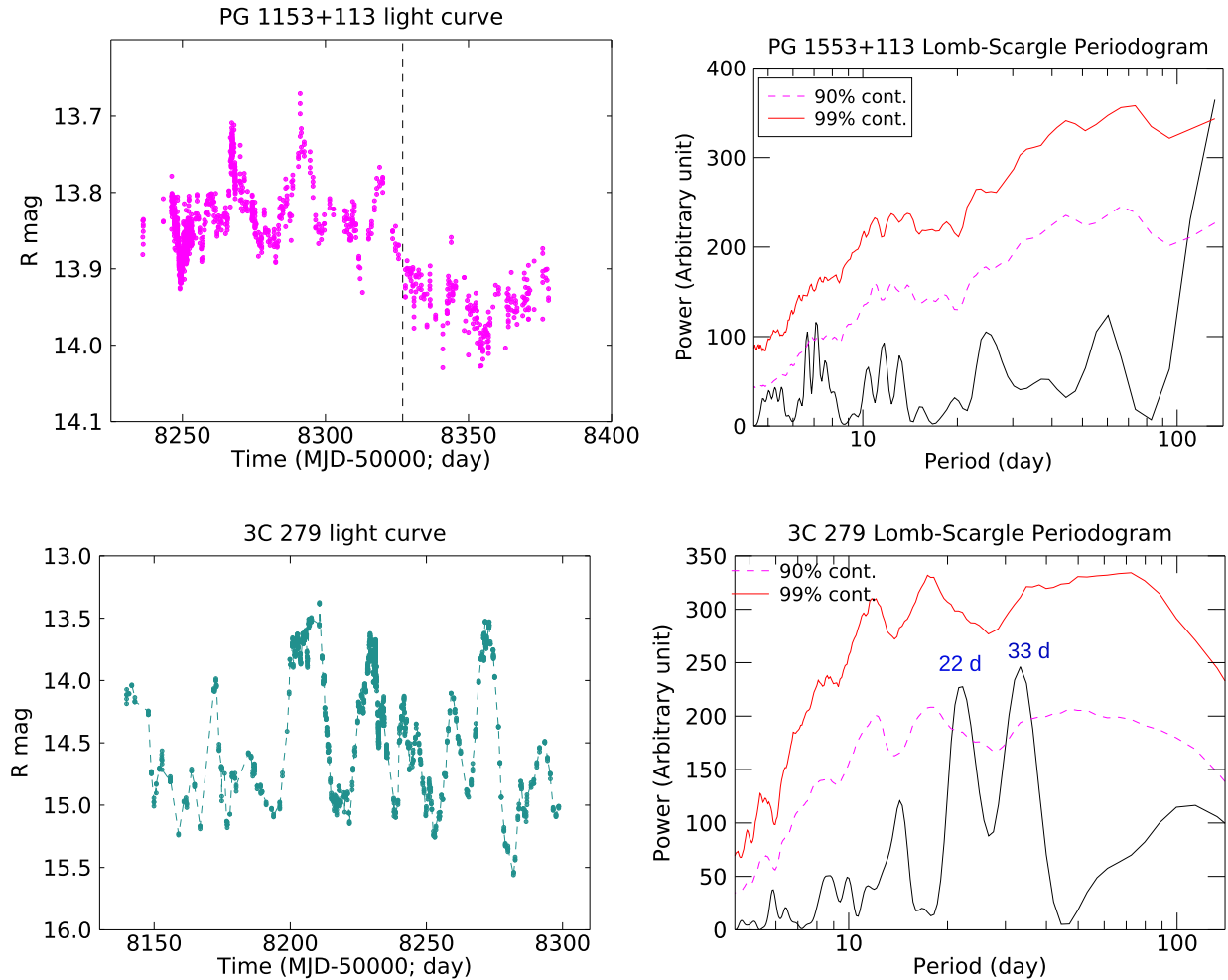


**Figure 3.** LSP and the R band light curve of the blazars PG 1553+113 and 3C 279 are shown in the top and bottom panels, respectively. The 90 and 99 per cent significance contours from simulation are shown on the LSP diagram by magenta and red curves, respectively.

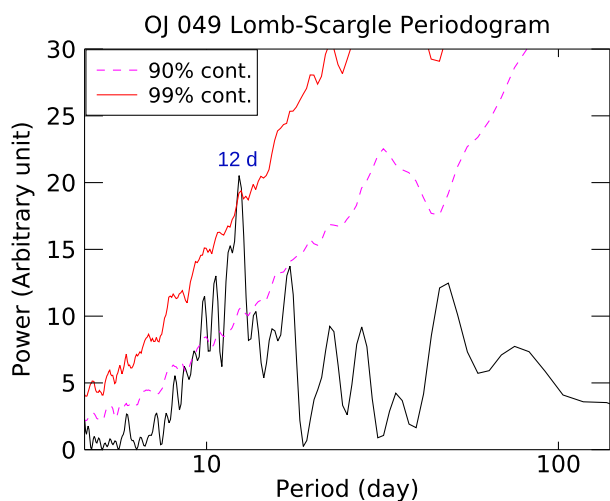


**Figure 4.** LSP of the blazar OJ 49 showing possible  $12 \pm 1.5$  d periodicity. The 90 and 99 per cent significance contours from simulation are shown by the magenta and red curves, respectively.

of these flares could be extrinsic and intrinsic in nature, as discussed qualitatively in the following sections.

### 5.1 Source intrinsic scenario

The flares in blazars can be explained in the context of internal shocks propagating along the blazar relativistic jets. As an illustrative example of blazar flares which lasts about a week, here we attempt to produce a flare using the method worked out by Kirk, Rieger & Mastichiadis (1998). This provides a framework for time-dependent analysis of the homogeneous single zone leptonic model, in which variable emission leading to large flares in the source flux is expected owing to gradual particle acceleration at the shock front and subsequent radiative cooling at the emission region. The model assumes that the shocks are propagating along a cylindrical jet aligned near the line of sight, and that particles injected at a constant rate at the shock wavefront lose energy primarily via synchrotron emission.

The evolution of the particles in the acceleration zone is given by the diffusion equation,

$$\frac{\partial N}{\partial t} + \frac{\partial}{\partial \gamma} \left[ \left( \frac{\gamma}{t_{acc}} - \beta_s \gamma^2 \right) N \right] + \frac{N}{t_{acc}} = Q \delta(\gamma - \gamma_0), \quad (8)$$

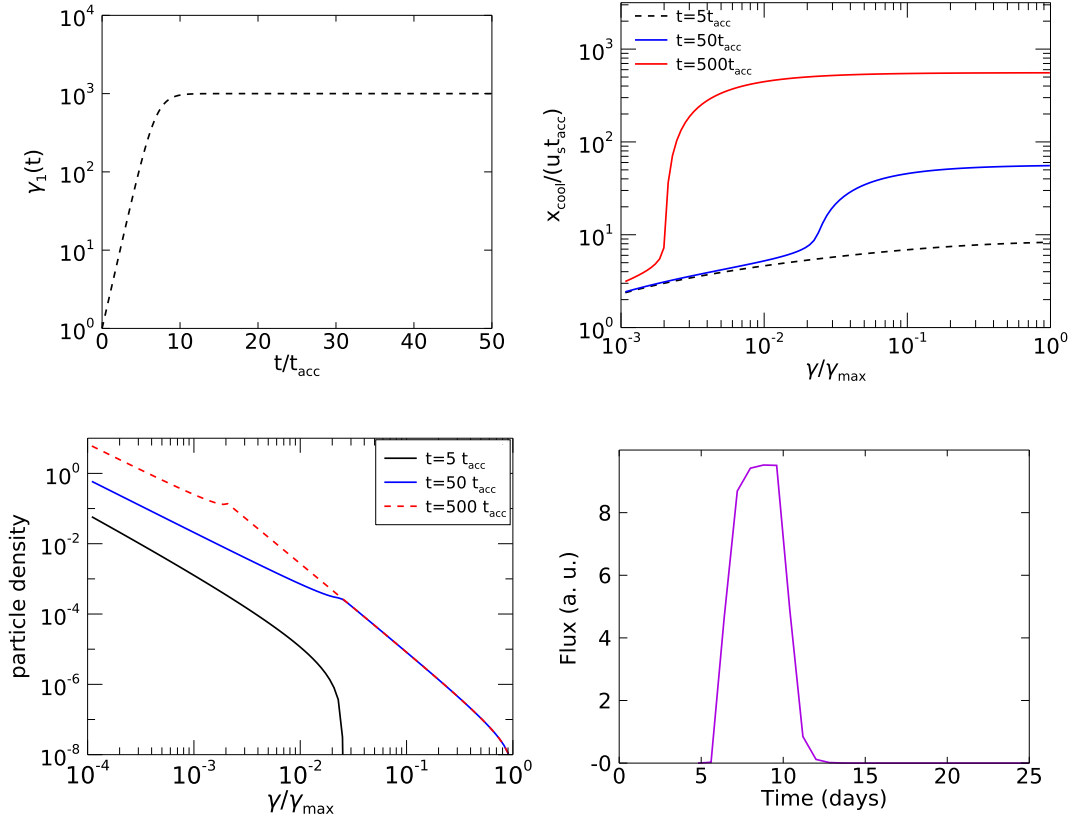


**Figure 5.** *Top:* Time evolution of maximum electron Lorentz factor as it accelerates (left-hand panel). Cooling length behind the shock wave front as a function of electron energy for three different times. *Bottom:* The normalized integrated particle (electron) density in the acceleration zone for three different times  $5 t_{acc}$ ,  $50 t_{acc}$ , and  $500 t_{acc}$  as shown by the black, blue, and red curves, respectively (left-hand panel). Rise and decay of the blazar emission due to particles accelerated at the relativistic shocks front and thereby cooling, respectively (right-hand panel).

where  $\beta_s \gamma^2$  represents the loss of the energy by the synchrotron radiation with

$$\beta_s = \frac{4}{3} \frac{\sigma_T}{m_e c^2} \left( \frac{B^2}{2\mu_0} \right), \quad (9)$$

where  $\sigma_T$ ,  $B$  and  $\mu_0$  are the Thompson-scattering cross-section, the magnetic field, and the permeability of free space, respectively.

Particle acceleration reaching up to  $\gamma_{max} = (\beta_s t_{acc})^{-1}$  is described by the equation

$$\gamma_1(t) = \left( \frac{1}{\gamma_{max}} + \left[ \frac{1}{\gamma_0} - \frac{1}{\gamma_{max}} \right] e^{-t/t_{acc}} \right)^{-1}, \quad (10)$$

which shown in the top panel of Fig. 5. The distributions of the (normalized) particle densities over the particle energies for the three different acceleration times, i.e. 5, 50, and 500  $t_{acc}$  are presented in the bottom left panel of Fig. 5 (see similar fig. 1 in Kirk et al. 1998). The breaks which naturally appear in the curves divide the population into particles with energies greater than those which cool within the source and low energy particles which do not cool within the emission region.

The particle enhancement in the regions is described by the equations,  $Q(t) = Q_0$  for  $t < 0$  and  $t > t_f$  and  $Q(t) = (1 + \eta_f) Q_0$  for  $0 < t < t_f$ .

We have then,

$$I(\nu, t) = I_1(\nu, t) + \eta_f [I_1(\nu, t) - I_1(\nu, (1 - u_s/c)t_f)]. \quad (11)$$

For small angles  $\cos\theta \sim 1$ , and  $\delta \sim 2\Gamma$  such that the relations  $I(\nu, t) = \delta^3 I(\nu', t')$ ,  $\nu = \Gamma(1 + \beta) \approx 2\Gamma\nu'$  are used to

transform the source rest-frame quantities (primed) to the observer's frame (unprimed). We take  $\nu = 4.55 \times 10^{14}$  Hz, the frequency corresponding to the mean effective wavelength of R-band (658 nm) and the shocks travelling down the blazar jet with relativistic speeds ( $\beta_s = 0.1$ ). The resulting normalized intensity profile mimicking the flaring behaviour observed in the blazars is presented in the bottom right panel of Fig. 5.

## 5.2 Source extrinsic scenario

A large flare in the blazar flux can also appear owing to the Doppler boosted emission when the emission regions travel along a curve trajectory in the jets. In such cases, the rest-frame flux ( $F'_{\nu}$ ) is related to the observed flux ( $F_{\nu}$ ) through the equations

$$\frac{F_{\nu}(\nu)}{F'_{\nu}(\nu)} = \delta^{3+\alpha} \quad \text{and} \quad \delta(t) = \frac{1}{\Gamma(1 - \beta \cos\theta)}. \quad (12)$$

The optical spectral slope is, in general, larger than 1 in LSPs, (in our case, OJ 49, S4 0954+658, TXS 1156+295, and 3C 279) and less than 1 in case of HSPs (here, PG1553+113). For illustrative purposes, however, here the spectral index is taken as  $\alpha \sim 1$ . If we assume the apparent flux rise happens purely due to the changes in the Doppler factor ( $\delta$ ), which further can be related to the changes in the angle with the line of sight or/and the changes in the bulk Lorentz factor. Here as an illustration, we treat two cases considering change in  $\theta$  and  $\Gamma$  separately.

- (i) Change in the angle of the line of sight:



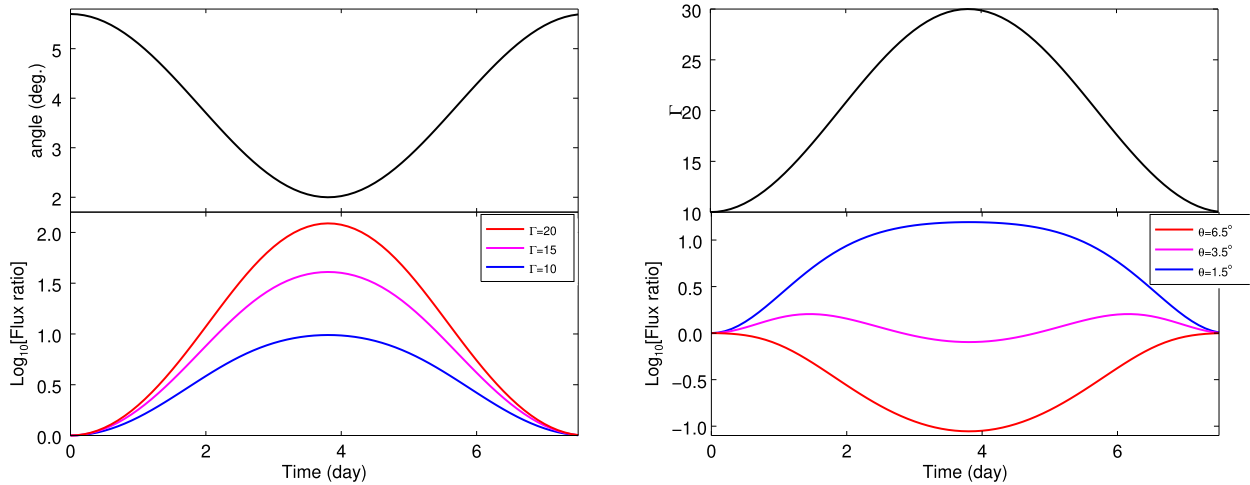


**Figure 6.** *Left:* As the angle between the emission region and the line of sight decreases (top panel), the flux appears to flare as a result of relativistic beaming (bottom panel). The three curves correspond to the three different values of the bulk Lorentz factors. *Right:* Similarly, flaring of flux (bottom panel) owing to the increase in the bulk Lorentz factor (top panel). The three curves correspond to the three different values of the angles of sight.

The angle between the emission region and the line of sight is allowed to gradually decrease, as approximated by  $\theta = \theta_0 - A \sin^2 \omega t$ , where  $\theta_0 = 5.7$  and  $A = 3.7$  as shown in the top left panel of Fig. 6. The resulting flux rise profiles for the three values of the bulk Lorentz factor, i.e.  $\Gamma = 10, 15,$  and  $20$  represented by the blue, magenta, and red curves, respectively, are shown in the lower left panel of Fig. 6. Furthermore to approximate the flaring behaviour that last about a week in the observer’s frame,  $\omega$  was chosen to be  $15 \times 10^{-6} \text{ rad s}^{-1}$ .

(ii) Change in  $\Gamma$  :

The bulk Lorentz factor of the dominant emission region is allowed to gradually increase, as approximated by  $\Gamma = \Gamma_0 + A \sin^2 \omega t$ , with  $\Gamma_0 = 10$  and  $A = 20$ , so that the plasma blob travelling at a speed of  $\Gamma = 10$  accelerates to attain  $\Gamma = 30$  and subsequently decelerates back to the previous speed. The evolution of  $\Gamma$  in time can be seen in the top right panel of Fig. 6. As in the previous case, the value of  $\omega$  was chosen to be  $15 \times 10^{-6} \text{ rad s}^{-1}$  such that the event lasts about a week in the observer’s frame. The resulting flux rise profiles for the three values of the angles of the line of sights, i.e.  $\theta = 1.5, 3.5,$  and  $6.5^\circ$  are represented by the blue, magenta, and red curves, respectively, shown in the lower right panel of Fig. 6.

### 5.3 Stochastic flux variability and possible periodicity

Blazars exhibit complex flux variability patterns with a possible mixture of several components such as general stochastic fluctuations, occasional large amplitude flares and possible QPOs arising from various instabilities both in the disc and the jet. The general aperiodic and stochastic variability observed in MWL observations of AGN is largely represented by red-noise (e.g. see Kelly, Sobolewska & Siemiginowska 2011; Isobe et al. 2015; Bhatta & Dhital 2020). The spectral power density of such variability is most consistent with a single power-law model, with negative spectral index ranging from  $\sim 1-2$ . A negative power-law implies that the variability power grows towards longer time-scales, meaning the source fluxes vary by larger amplitudes over yearly time-scales compared to shorter ones, i.e. intraday, daily, weekly, and monthly time-scales. However, it is interesting to note that in the particular case of the 3C 279 light curve in the bottom left panel of Fig. 3, the mean flux nearly remains stationary while the shorter term flux fluctuates rapidly. Similar observations can be made about PG 1153+113 when considering

only the light curve before the vertical dashed line. It is only when we consider the full-length light curve that the longer term variability appears dominant. It is possible that the processes driving variability which can be characterized by a negative power-law index are distinct in origin compared to the commonly observed variability characterized by positive power-law index. They could be signatures of the quasi-stationary isolated events which gets mixed with the general red-noise like variability.

Apart from the general aperiodic variability, LSP analysis of the light curves revealed hints of QPOs in some of the sources. However, the estimated significance of the peaks in the periodogram is moderate at about 90 per cent. Nevertheless, it is important to note that in blazar light curves heavily dominated by red noise, the actual QPO signals could appear relatively weak (see discussion in Bhatta & Dhital 2020). The periodicity analysis indicates that in blazar 3C 279 the two periods, well above 90 per cent significance level, appear to be in a 3:2 ratio. In X-ray binaries such as QPOs with periods in a 3:2 ratio are interpreted in terms of resonant oscillations of accretion flow (e.g. Kluźniak & Abramowicz 2005). Blazar QPOs on time-scales of a few months are relatively rare, although yearly time-scales QPOs have been reported in several blazars. Note that although QPOs in a time-scales of a few days are more likely to originate at the accretion disc, we detect them through the jet emission. Possible interpretations of the blazar QPO are discussed in detail in our previous works (see Bhatta 2017, 2019; Bhatta & Dhital 2020, and references therein).

## 6 CONCLUSION

A variability study was carried out using optical observations of the blazars 3C 279, OJ 49, S4 0954+658, TXS 1156+295, and PG 1553+113 spanning several weeks. The light curves using observations acquired through our ground based telescope networks showed some of the extraordinary flaring events in which a flux change of nearly 10 times was observed within a time-scale of  $\sim 10$  d. Flares in the sources OJ 49, S4 0954+658, and TXS 1156+295 were studied using a functional form of exponential rise and decay. Of these sources, slightly asymmetric flares of comparable normalized amplitude of  $\sim 8$  were observed in the blazars OJ 49, S4 0954+658; whereas light curves of the source TXS 1156+295 revealed a

fasted flux decay by  $\sim 11$  normalized amplitudes within the time-scale of four days. Such a rapid, large amplitude flux change reflects the most violent processes in the jet, e.g. shock waves and magnetic re-connection events. To explain the observed flares, qualitative descriptions of possible intrinsic and extrinsic scenarios were presented. In the source-intrinsic scenario, particle injection at the shock wave front can result in a flare in the source flux; whereas in the extrinsic scenario turbulent flow in the jet might lead to a change in the Doppler factor of a single, dominant energized cell, such that a slight change in the speed or angle to the line of sight can yield a large observed change in flux.

Furthermore, periodicity analysis was performed on the sources 3C 279, OJ 49, TXS 1156+295, and PG 1553+113 using LSPs supplemented by a large number of simulated light curves generated using Monte Carlo methods. The result indicated that a strong spectral peak was detected at the characteristic time-scale of  $\sim 12$  d to above 99 per cent significance level against power-law noise. In addition, two potentially significant periods 33 and 22 d, at a ratio of 3:2, were found to be detected at a significance level of  $\sim 95$  per cent.

## ACKNOWLEDGEMENTS

We are grateful to the anonymous reviewer for their constructive comments, which helped improve the quality of the paper significantly. We acknowledge the support of the Polish National Science Centre through the grants UMO-2017/26/D/ST9/01178 (GB), 2018/29/B/ST9/01793 (SZ), and 2020/39 / B / ST9 / 01398 (DG). KM acknowledges JSPS KAKENHI grant number 19K03930.

## DATA AVAILABILITY

The data used in this work can be shared on reasonable request to the corresponding author.

## REFERENCES

- Abdo A. A. et al., 2010a, *ApJ*, 716, 30  
 Abdo A. A. et al., 2010b, *ApJ*, 722, 520  
 Abeysekara A. U. et al., 2018, *ApJ*, 856, 95  
 Acciari V. A. et al., 2020, *ApJS*, 248, 29  
 Ackermann M. et al., 2015, *ApJ*, 813, L41  
 Agarwal A. et al., 2019, *MNRAS*, 488, 4093  
 Agudo I. et al., 2011, *ApJ*, 735, L10  
 Aharonian F. A., 2000, *New Astron.*, 5, 377  
 Aharonian F. et al., 2006, *A&A*, 448, L19  
 Albert J. et al., 2007, *ApJ*, 654, L119  
 Aleksić J. et al., 2015, *A&A*, 573, A50  
 Aliu E. et al., 2015, *ApJ*, 799, 7  
 Antonucci R. R. J., Ulvestad J. S., 1985, *ApJ*, 294, 158  
 Baloković M. et al., 2016, *ApJ*, 819, 156  
 Beckmann V. et al., 2002, *A&A*, 383, 410  
 Bhatta G. et al., 2016a, *ApJ*, 831, 92  
 Bhatta G., 2017, *ApJ*, 847, 7  
 Bhatta G., 2021, *ApJ*, 923, 7  
 Bhatta G., Dhital N., 2020, *ApJ*, 891, 120  
 Bhatta G., Mohorian M., Bilinsky I., 2018, *A&A*, 619, A93  
 Bhatta G., Webb J., 2018, *Galaxies*, 6, 2  
 Bhatta G. et al., 2016b, *ApJ*, 832, 47  
 Blandford R., Eichler D., 1987, *Phys. Rep.*, 154, 1  
 Blinov D. et al., 2018, *MNRAS*, 474, 1296  
 Böttcher M. et al., 2007, *ApJ*, 670, 968  
 Bromberg O., Levinson A., 2009, *ApJ*, 699, 1274  
 Burbidge G. R., Jones T. W., Odell S. L., 1974, *ApJ*, 193, 43  
 Chatterjee R. et al., 2013, *ApJ*, 763, L11  
 Danforth C. W., Keeney B. A., Stocke J. T., Shull J. M., Yao Y., 2010, *ApJ*, 720, 976  
 Dermer C. D., Schlickeiser R., Mastichiadis A., 1992, *A&A*, 256, L27  
 Dodson R. et al., 2008, *ApJS*, 175, 314  
 Falomo R., Treves A., 1990, *PASP*, 102, 1120  
 Fan J. H. et al., 2006, *PASJ*, 58, 797  
 Ghisellini G., Madau P., 1996, *MNRAS*, 280, 67  
 Giannios D., 2013, *MNRAS*, 431, 355  
 Giannios D., Uzdensky D. A., 2019, *MNRAS*, 484, 1378  
 Guo X., Sironi L., Narayan R., 2014a, *ApJ*, 797, 47  
 Guo X., Sironi L., Narayan R., 2014b, *ApJ*, 794, 153  
 Hagen-Thorn V. A. et al., 2015, *Astron. Rep.*, 59, 551.  
 Hallum M. K. et al., 2022, *ApJ*, 926, 180  
 Hayashida M. et al., 2015, *ApJ*, 807, 79  
 Heidt J., Wagner S. J., 1996, *A&A*, 305, 42  
 Hewett P. C., Wild V., 2010, *MNRAS*, 405, 2302  
 Hughes P. A., Aller H. D., Aller M. F., 1998, *ApJ*, 503, 662  
 IceCube Collaboration, 2018, *Science*, 361, eaat1378  
 Isobe N. et al., 2015, *ApJ*, 798, 27  
 Jorstad S. G. et al., 2001, *ApJS*, 134, 181  
 Jorstad S. G. et al., 2004, *AJ*, 127, 3115  
 Jorstad S. G. et al., 2005, *AJ*, 130, 1418  
 Jorstad S. G. et al., 2013, *ApJ*, 773, 147  
 Jorstad S. G. et al., 2017, *ApJ*, 846, 98  
 Jorstad S., Marscher A., 2016, *Galaxies*, 4, 47  
 Kellermann K. I. et al., 2004, *ApJ*, 609, 539  
 Kelly B. C., Sobolewska M., Siemiginowska A., 2011, *ApJ*, 730, 52  
 Kirk J. G., Rieger F. M., Mastichiadis A., 1998, *A&A*, 333, 452  
 Kluźniak W., Abramowicz M. A., 2005, *Ap&SS*, 300, 143  
 Larionov V. M. et al., 2008, *A&A*, 492, 389  
 Lind K. R., Blandford R. D., 1985, *ApJ*, 295, 358  
 Lister M. L., Marscher A. P., Gear W. K., 1998, *ApJ*, 504, 702  
 Lomb N. R., 1976, *Ap&SS*, 39, 447  
 MAGIC Collaboration, 2008, *Science*, 320, 1752  
 Mannheim K., 1993, *A&A*, 269, 67  
 Maraschi L., Ghisellini G., Celotti A., 1992, *ApJ*, 397, L5  
 Marscher A. P. et al., 2010, *ApJ*, 710, L126  
 Marscher A. P., 2014, *ApJ*, 780, 87  
 Marscher A. P., Gear W. K., 1985, *ApJ*, 298, 114  
 Meng N., Zhang X., Wu J., Ma J., Zhou X., 2018, *ApJS*, 237, 30  
 Morozova D. A. et al., 2014, *AJ*, 148, 42.  
 Morozova D. et al., 2016, *Galaxies*, 4, 24.  
 Mücke A., Protheroe R. J., Engel R., Rachen J. P., Stanev T., 2003, *Astropart. Phys.*, 18, 593  
 Mukherjee R., VERITAS Collaboration, 2017, *Astron. Telegram*, 11075  
 Nalewajko K. et al., 2011, *MNRAS*, 413, 333  
 Narayan R., Piran T., 2012, *MNRAS*, 420, 604  
 Nilsson K. et al., 2018, *A&A*, 620, A185  
 Osterman M. A. et al., 2006, *AJ*, 132, 873  
 Paliya V. S. et al., 2016, *ApJ*, 817, 61  
 Pandey A., Gupta A. C., Wiita P. J., Tiwari S. N., 2019, *ApJ*, 871, 192  
 Papadakis I. E. et al., 2004, *A&A*, 426, 437  
 Park J. et al., 2019, *ApJ*, 877, 106  
 Pursimo T. et al., 2017, *Astron. Telegram*, 10948  
 Raiteri C. M. 2017, *Nature*, 552, 374  
 Raiteri C. M. et al., 1999, *A&A*, 352, 19.  
 Raiteri C. M. et al., 2015, *MNRAS*, 454, 353  
 Rajput B., Pandey A., 2021, *Galaxies*, 9, 118  
 Rieger F. M., Mannheim K., 2000, *A&A*, 359, 948  
 Scargle J. D., 1982, *ApJ*, 263, 835  
 Sheng Y. et al., 2022, preprint (arXiv:2209.09877)  
 Sikora M., Begelman M. C., Rees M. J., 1994, *ApJ*, 421, 153  
 Sitko M. L., Schmidt G. D., Stein W. A., 1985, *ApJS*, 59, 323  
 Smith P. S. et al., 1987, *ApJS*, 64, 459  
 Spruit H. C., Daigne F., Drenkhahn G., 2001, *A&A*, 369, 694

- Urry C. M., Padovani P., 1995, *PASP*, 107, 803  
Vaughan S., 2005, *A&A*, 431, 391  
Vaughan S., Edelson R., Warwick R. S., Uttley P., 2003, *MNRAS*, 345, 1271  
Vlasyuk V. V. et al., 2022, *Astron. Telegram*, 15376  
Wehrle A. E. et al., 2012, *ApJ*, 758, 72  
Zola S. et al., 2016, *Galaxies*, 4, 41  
Zola S. et al., 2021, *Rev. Mex. Astron. Astrofis*, 53, 206

This paper has been typeset from a  $\text{\TeX/L\AA\TeX}$  file prepared by the author.